

Hot neutron stars with microscopic equations of state

Jia-Jing Lu (陆家靖)^{1,2}, Zeng-Hua Li (李增花)^{1,*}, G. F. Burgio², and H.-J. Schulze²

¹*Institute of Modern Physics, Key Laboratory of Nuclear Physics and*

Ion-beam Application (MOE), Fudan University, Shanghai 200433, P.R. China

²*INFN Sezione di Catania, Dipartimento di Fisica, Università di Catania, Via Santa Sofia 64, 95123 Catania, Italy*

(Dated: July 9, 2019)

We study the properties of hot beta-stable nuclear matter using equations of state derived within the Brueckner-Hartree-Fock approach at finite temperature including consistent three-body forces. Simple and accurate parametrizations of the finite-temperature equations of state are provided. The properties of hot neutron stars are then investigated within this framework, in particular the temperature dependence of the maximum mass. We find very small temperature effects and analyze the interplay of the different contributions.

I. INTRODUCTION

The recent first observation of a neutron star (NS) merger event, GW170817 [1], has opened new possibilities to understand the properties of the extremely hot and dense environment that is created by the fusion of two NSs, and represents a transitory state to either collapse to a black hole or the formation of a very heavy NS [2, 3].

The theoretical modeling of this system requires first of all the knowledge of the nuclear equation of state (EOS) under the extreme conditions of several times normal nuclear matter density $\rho_0 \approx 0.17 \text{ fm}^{-3}$, and temperatures of tens of MeV. It is the motivation of this work to provide realistic microscopically founded EOSs for this purpose. We will therefore extend to finite temperature several microscopic EOSs that have been derived within the Brueckner-Hartree-Fock (BHF) formalism [4–6] based on realistic two-nucleon and three-nucleon forces [7–9]. They feature reasonable properties at (sub)nuclear densities in agreement with nuclear-structure phenomenology [9–11], and are also fully compatible with recent constraints obtained from the analysis of the GW170817 event [12].

Apart from the application to simulations of merger events, such finite-temperature EOSs are also relevant for the modeling of compact stellar objects like proton-neutron stars [13–17] and supernovae [18].

A particularly important feature of any NS EOS is the associated maximum stable NS mass. Currently a lower limit for the cold EOS is due to the observation of NSs with above two solar masses [19], recently updated to $M_{\text{max}} > 2.17 \pm 0.1 M_{\odot}$ [20], whereas the analysis of GW170817 (in particular its delayed decay to a black hole) has permitted to establish approximate upper limits of about $2.2 M_{\odot}$ [21] for the maximum mass of a static cold NS. Two important physical effects influence the estimate of the maximum mass of a cold static NS from the properties of the transient object (hypermassive NS) created by the merger: First, the remnant is (differentially) rotating fast, which allows temporarily a higher metastable mass (of about 20 percent) than for the nonrotating object [22–25]. Second, the remnant is hot, and therefore its maximum mass is different from the one of the cold object. For this estimate the temperature dependence of the EOS becomes essential.

There is therefore a possible mass range of the hot rotating transitory metastable object that depends on the finite-temperature EOS. Of course the precise determination of this feature requires sophisticated simulations [26–29] and we will in this article only give very simple estimates of the effect, using and comparing our different EOSs.

A few finite-temperature nuclear EOSs for astrophysical simulations are now available [16, 17, 30–36], and the predictions for the effects of temperature on stellar stability are conflicting: Relativistic-mean-field (RMF) models usually predict increasing stability (maximum mass) with temperature [14, 37, 38], whereas BHF results [16, 17] indicate in general a slight reduction of the maximum mass. We will try to analyze in some detail this feature.

Our paper is organized as follows. In Sec. II A we discuss the finite-temperature BHF approach and the fits of our finite-temperature results for the free energy. The composition of stellar matter and the EOS are presented in Sec. II B, along with the equations of stellar structure. The numerical results regarding temperature effects on EOS and maximum mass are then illustrated in Sec. III, and conclusions are drawn in Sec. IV.

II. FORMALISM

A. Brueckner-Bethe-Goldstone theory at finite temperature

The free energy density of hot nuclear matter consists of two contributions,

$$f = f_N + f_L, \quad (1)$$

where f_N is the nucleonic part and f_L denotes the contribution of leptons e, μ, ν_e, ν_{μ} , and their antiparticles. In the present work, we employ the BHF approach for asymmetric nuclear matter at finite temperature [5, 16, 17, 39–41] to calculate the nucleonic contribution. The essential ingredient of this approach is the interaction matrix K , which satisfies the self-consistent equations

$$K(\rho, x_p; E) = V + V \text{Re} \sum_{1,2} \frac{|12\rangle(1-n_1)(1-n_2)\langle 12|}{E - e_1 - e_2 + i0} K(\rho, x_p; E) \quad (2)$$

* zhli09@fudan.edu.cn

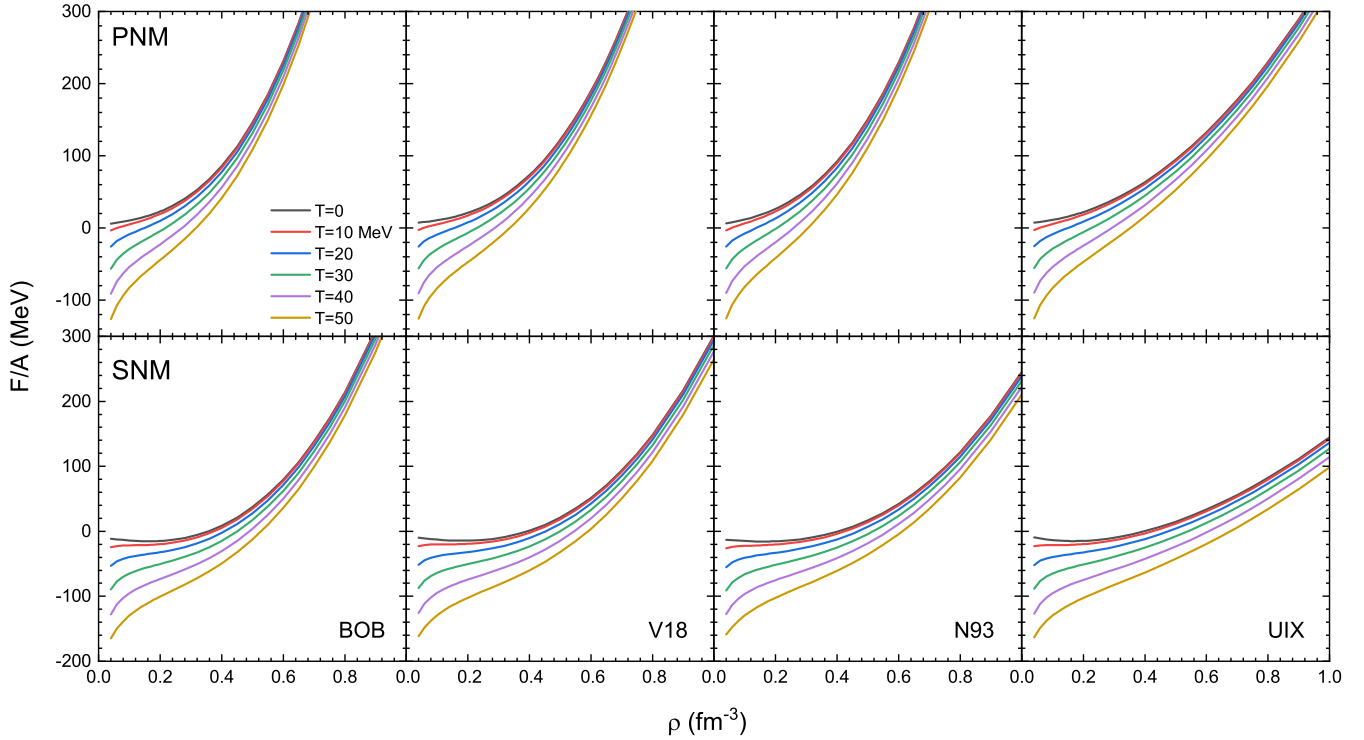


FIG. 1. Free energy per nucleon as a function of nucleon density for symmetric (lower panels) and pure neutron (upper panels) matter with different EoSs, for temperatures ranging from 0 to 50 MeV in steps of 10 MeV.

and

$$U_1(\rho, x_p) = \text{Re} \sum_2 n_2 \langle 12 | K(\rho, x_p; e_1 + e_2) | 12 \rangle_a, \quad (3)$$

where $x_p = \rho_p/\rho$ is the proton fraction, and ρ_p and ρ are the proton and the total baryon density, respectively. E is the starting energy and $e(k) \equiv k^2/2m + U(k)$ is the single-particle (s.p.) energy. The multi-indices 1,2 denote in general momentum, isospin, and spin.

Several choices for the realistic nucleon-nucleon (NN) interaction V are adopted in the present calculations [9]: the Argonne V_{18} [42], the Bonn B (BOB) [43], and the Nijmegen 93 (N93) [44], and compatible three-nucleon forces as input. More precisely, the BOB and N93 are supplemented with microscopic TBF employing the same meson-exchange parameters as the two-body potentials [8, 9, 45], whereas V_{18} is combined either with a microscopic or a phenomenological TBF, the latter consisting of an attractive term due to two-pion exchange with excitation of an intermediate Δ resonance, and a repulsive phenomenological central term [7, 46]. They are labeled as V18 and UIX, respectively, throughout the paper and in all figures. The TBF are reduced to an effective two-body force and added to the bare potential in the BHF calculation, see Refs. [8, 9, 45] for details.

At finite temperature, $n(k)$ in Eqs. (2) and (3) is a Fermi distribution. For a given density and temperature, these equations have to be solved self-consistently along with the following equations for the auxiliary chemical potentials $\tilde{\mu}_{n,p}$,

$$\rho_i = 2 \sum_k n_i(k) = 2 \sum_k \left[\exp\left(\frac{e_i(k) - \tilde{\mu}_i}{T}\right) + 1 \right]^{-1}. \quad (4)$$

To save computational time and simplify the numerical procedure, in the following we employ the so-called frozen-correlations approximation [16, 41], i.e., the correlations at $T \neq 0$ are assumed to be essentially the same as at $T = 0$. This means that the s.p. potential $U_i(k)$ for the component i at finite temperature is approximated by the one calculated at $T = 0$. Within this approximation, the nucleonic free energy density has the following simplified expression,

$$f_N = \sum_{i=n,p} \left[2 \sum_k n_i(k) \left(\frac{k^2}{2m_i} + \frac{1}{2} U_i(k) \right) - T s_i \right], \quad (5)$$

where

$$s_i = -2 \sum_k \left(n_i(k) \ln n_i(k) + [1 - n_i(k)] \ln [1 - n_i(k)] \right) \quad (6)$$

is the entropy density for the component i treated as a free Fermi gas with spectrum $e_i(k)$. It turns out that the assumed independence is valid to a good accuracy [16, 41], at least for not too high temperature, $T \lesssim 30$ MeV.

We stress that the BHF approximation, both at zero and finite temperature, does not fulfill the Hugenholtz-Van Hove theorem [41], and therefore the following procedure has to be adopted in order to derive all necessary thermodynamical quantities in a consistent way from the total free energy density f , namely one defines the “true” chemical potentials μ_i ,

pressure p , and internal energy density ε as

$$\mu_i = \frac{\partial f}{\partial \rho_i}, \quad (7)$$

$$p = \rho^2 \frac{\partial(f/\rho)}{\partial \rho} = \sum_i \mu_i \rho_i - f, \quad (8)$$

$$\varepsilon = f + Ts, \quad s = -\frac{\partial f}{\partial T}. \quad (9)$$

For illustration, we display in Fig. 1 the nucleonic free energy per nucleon, $F/A = f_N/\rho$, as a function of the baryon density ρ , obtained following the above discussed procedure, for symmetric nuclear matter ($x_p = 1/2$, SNM) and pure neutron matter ($x_p = 0$, PNM), and the different EOSs we are using, for several values of temperature between 0 and 50 MeV. At $T = 0$ the free energy coincides with the internal energy and the corresponding SNM curve is just the usual nuclear matter saturation curve. The temperature effect is less pronounced for PNM due to the larger Fermi energy of the neutrons at given density. We notice that the results are ordered with increasing stiffness of the EOS as UIX, N93, V18, BOB.

For practical use, we provide analytical fits of the free energy $F/A(\rho, T)$ for SNM and PNM. We find that in both cases the following functional forms provide excellent parametrizations of the numerical results in the required ranges of density ($0.05 \text{ fm}^{-3} \lesssim \rho \lesssim 1 \text{ fm}^{-3}$) and temperature ($5 \text{ MeV} \leq T \leq 50 \text{ MeV}$):

$$\frac{F}{A}(\rho, T) = a\rho + b\rho^c + d + \tilde{a}t^2\rho + \tilde{b}t^2 \ln(\rho) + (\tilde{c}t^2 + \tilde{d}t^{\tilde{e}})/\rho, \quad (10)$$

where $t = T/(100 \text{ MeV})$ and F/A and ρ are given in MeV and fm^{-3} , respectively. The parameters of the fits are listed in Table I for the different EOSs we are using. The rms deviations of fits and data are better than 1 MeV for all EOSs.

For the asymmetric matter case, it turns out that the dependence on proton fraction can be very well approximated by a parabolic law, as at zero temperature [17, 47]:

$$\frac{F}{A}(\rho, T, x_p) \approx \frac{F}{A}(\rho, T, 0.5) + (1 - 2x_p)^2 \left[\frac{F}{A}(\rho, T, 0) - \frac{F}{A}(\rho, T, 0.5) \right]. \quad (11)$$

Therefore, for the treatment of the beta-stable case, it is only necessary to provide parametrizations for SNM and PNM. For convenience we provide in the supplemental material [48] the complete EOS tables in the parameter space of temperature, baryon density, and proton fraction.

B. Composition and EOS of hot stellar matter

The purpose of this article is to evaluate the effect of the intrinsic temperature dependence of the nuclear EOS caused by the strong interaction. However, finite temperature also affects the composition of stellar matter governed by the weak interaction. In this article we study exclusively beta-stable and

TABLE I. Parameters of the fit for the free energy per nucleon F/A , Eq. (10), for symmetric nuclear matter (SNM) and pure neutron matter (PNM) and the different EOSs used.

		a	b	c	d	\tilde{a}	\tilde{b}	\tilde{c}	\tilde{d}	\tilde{e}
BOB	SNM	-65	498	2.67	-9	-124	203	-105	122	2.20
BOB	PNM	57	856	2.91	4	-85	152	-32	43	2.47
V18	SNM	-60	369	2.66	-8	-147	209	-66	85	2.32
V18	PNM	37	667	2.78	6	-91	154	-52	62	2.28
N93	SNM	-42	298	2.61	-12	-142	211	-64	87	2.35
N93	PNM	67	743	2.71	4	-95	154	-35	46	2.44
UIX	SNM	-174	323	1.61	-4	-186	199	-136	153	2.16
UIX	PNM	24	326	2.09	6	-117	153	-85	94	2.16

neutrino-free nuclear matter, assuming that the temporal evolution is slow enough to justify these assumptions. This might not necessarily be a good approximation for merger simulations [49].

In beta-stable nuclear matter the chemical potential of any particle $i = n, p, l$ is uniquely determined by the conserved quantities baryon number B_i , electric charge Q_i , and weak charges (lepton numbers) $L_i^{(e)}, L_i^{(\mu)}$:

$$\mu_i = B_i \mu_n + L_i^{(e)} \mu_{\nu_e} + L_i^{(\mu)} \mu_{\nu_\mu}. \quad (12)$$

For stellar matter containing nucleons and leptons as relevant degrees of freedom, the chemical equilibrium conditions read explicitly

$$\mu_n - \mu_p = \mu_e = \mu_\mu. \quad (13)$$

At given baryon density ρ , these equations have to be solved together with the charge-neutrality condition

$$\sum_i Q_i \rho_i = 0. \quad (14)$$

The various chemical potentials are obtained from the total free energy density f , Eq. (1),

$$\mu_i(\{\rho_j\}) = \left. \frac{\partial f}{\partial \rho_i} \right|_{\rho_j \neq i}. \quad (15)$$

Using the hadronic and leptonic chemical potentials, one can calculate the composition of beta-stable stellar matter, and then the total pressure p and the internal energy density ε , through the usual thermodynamical relations expressed by Eqs. (8,9). Once the EOS $p(\varepsilon)$ is specified, the stable configurations of a NS can be obtained from the well-known hydrostatic equilibrium equations of Tolman, Oppenheimer, and Volkov [50] for pressure $p(r)$, enclosed gravitational mass $m(r)$, and baryonic mass $m_B(r)$

$$\frac{dp}{dr} = -\frac{Gm\varepsilon}{r^2} \frac{(1 + p/\varepsilon)(1 + 4\pi r^3 p/m)}{1 - 2Gm/r}, \quad (16)$$

$$\frac{dm}{dr} = 4\pi r^2 \varepsilon, \quad (17)$$

$$\frac{dm_B}{dr} = 4\pi r^2 \frac{\rho m_N}{\sqrt{1 - 2Gm/r}}, \quad (18)$$

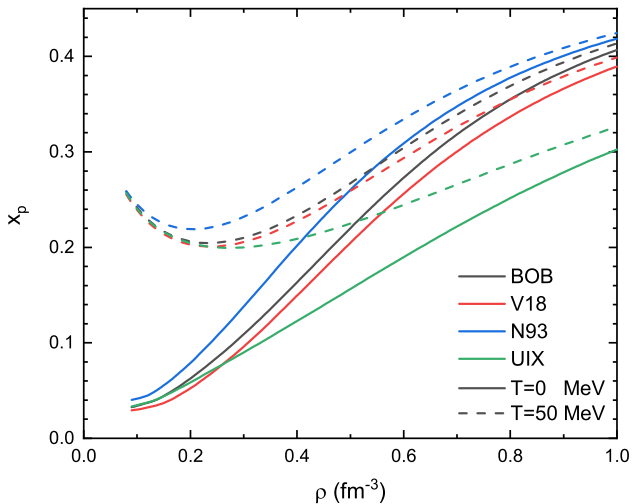


FIG. 2. Proton fractions in beta-stable matter at the temperatures $T = 0$ (solid curves) and 50 MeV (dashed curves) for the different EOSs.

where $m_N = 1.67 \times 10^{-24}$ g is the nucleon mass and $G = 6.67408 \times 10^{-8} \text{cm}^3 \text{g}^{-1} \text{s}^{-2}$ the gravitational constant. For a chosen central value of the energy density, the numerical integration of these equations provides the mass (M, M_B) – radius (R) relations.

The solution of these equations depends obviously on the temperature profile $T(r)$. In any realistic simulation of an astrophysical scenario at finite temperature (supernova, protoneutron star, merger), the TOV equations are therefore embedded in a detailed and self-consistent dynamical simulation of the temperature evolution. We cannot perform such detailed studies here, but our current aim is just to identify the global effect of finite temperature on the stability of a NS merger remnant, as motivated in the Introduction. This will serve as a preparation for a better qualitative understanding of future detailed simulations based on our finite-temperature EOSs.

We therefore assume simply a constant temperature inside the star and attach for the outer part a cold crust given in Ref. [51] for the medium-density regime ($0.001 \text{fm}^{-3} < \rho < 0.08 \text{fm}^{-3}$), and in Refs. [52, 53] for the outer crust ($\rho < 0.001 \text{fm}^{-3}$). The maximum-mass domain that we are interested in, is hardly affected by the structure of this low-density transition region [16, 17].

III. RESULTS

In the following we present the results of our numerical calculations regarding the composition of hot NS matter and the structure of NSs.

A. Composition of stellar matter

A main characteristic of stellar nuclear matter is its proton fraction, which is displayed in Fig. 2 as a function of the

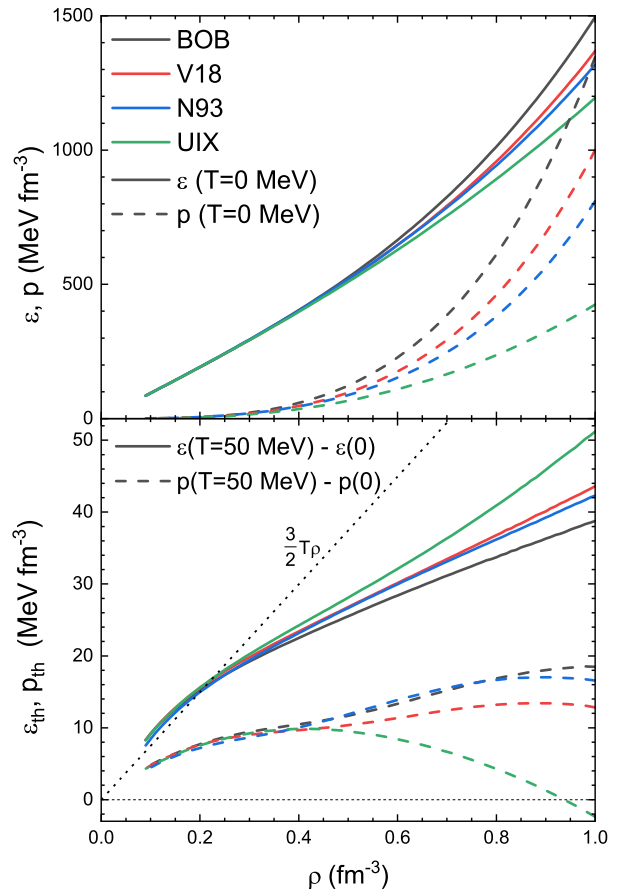


FIG. 3. Internal energy density ϵ (solid curves) and pressure p (dashed curves) of beta-stable matter at $T = 0$ (upper panel) and changes of those quantities at $T = 50$ MeV for the different EOSs (lower panel).

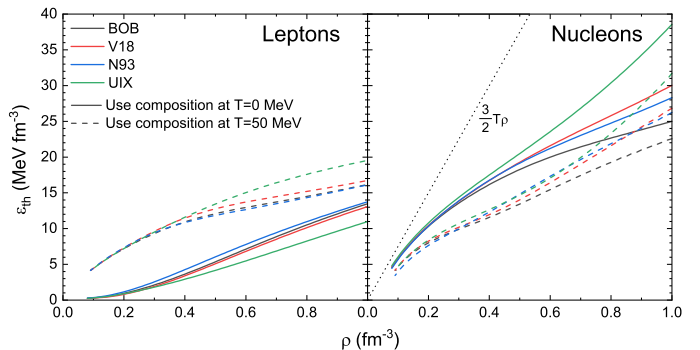


FIG. 4. Lepton and nucleon contributions to the thermal internal energy density of beta-stable matter at $T = 50$ MeV for the different EOSs. The solid (dashed) curves employ the particle fractions of cold (hot) matter, see Fig. 2.

baryon density for the temperatures $T = 0$ and 50 MeV, obtained with the different EOSs. We stress that both electrons and muons are taken into account for these results.

First we notice that the different EOSs predict somewhat different proton fractions at high density, but all of them exceed the threshold value $x_{\text{DU}} \approx 0.13$ for the opening of the direct Urca cooling reactions in cold matter. The onset den-

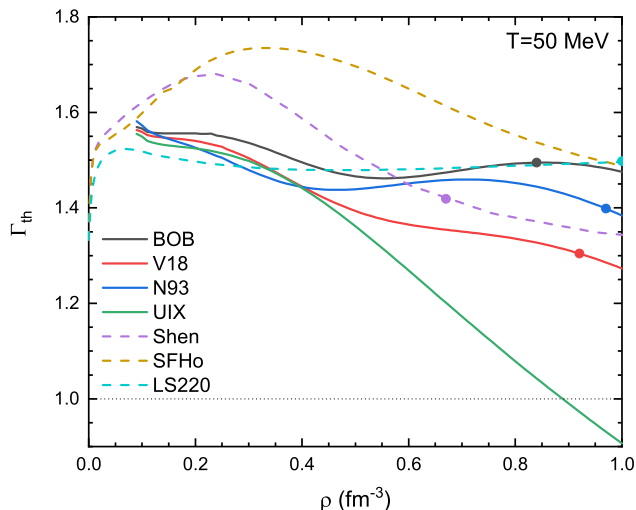


FIG. 5. Adiabatic index at $T = 50$ MeV obtained for different EOSs. The markers indicate the central densities of the maximum-mass stars. For this comparison (anti)muons have been disregarded in the stellar composition.

sity is comprised in the range $0.3\text{--}0.4\text{ fm}^{-3}$, and therefore medium-mass NS can cool down very rapidly, as illustrated in our recent work [54]. The predicted NS cooling properties with these EOSs are compatible with all current cooling data.

As far as the finite-temperature effects are concerned, we notice that the proton fraction is mainly affected in the low-density region, where leptons become rather numerous as a result of Fermi distributions at finite temperature. Because of the charge-neutrality condition, this increases the proton fraction and thus the isospin symmetry of nuclear matter, and this counteracts the stiffening of the EOS due to the individual thermal pressures of the nucleons. On the other hand, the increase of the lepton densities with temperature augments the thermal lepton pressure, which in turn acts against the effect of increasing isospin symmetry. We will analyze the interplay between these effects in the following.

B. Pressure and energy density

Fig. 3 shows the EOS of beta-stable matter $p(\rho)$ and $\varepsilon(\rho)$ obtained with the different EOSs at $T = 0$ in the upper panel and the changes at $T = 50$ MeV in the lower panel, i.e., the thermal pressure $p_{\text{th}}(T, \rho) \equiv p(T, \rho) - p(0, \rho)$ (dashed curves) and internal energy density $\varepsilon_{\text{th}}(T, \rho) \equiv \varepsilon(T, \rho) - \varepsilon(0, \rho)$ (solid curves). One can clearly see the nonmonotonic density behavior of the thermal pressure due to three competing effects: The individual thermal pressures of protons and neutrons at fixed partial densities are increasing, but the isospin asymmetry is decreasing with temperature (see Fig. 2), which reduces the total baryonic pressure. On the other hand, the increased lepton densities augment the lepton thermal pressure.

In our approach, the overall thermal effects are small, of the order of a few percent at high density, even at the fairly high

temperature $T = 50$ MeV considered here. In fact a simple nonrelativistic ideal-gas approximation for nucleons [55]

$$\varepsilon_{\text{th}} = \frac{3}{2} T \rho \quad (19)$$

(dotted curve in the lower panel of Fig. 3), significantly overestimates the thermal effects. This result is independent of the frozen-correlations approximation adopted here, as was demonstrated in Ref. [17].

In order to understand in some more detail the previous results, we show in Fig. 4 separately the lepton and nucleon contributions to the thermal energy density at $T = 50$ MeV, obtained in two different ways: The solid curves show the results obtained with the proton fractions of cold matter (solid curves in Fig. 2), whereas the dashed curves employ the consistent proton fractions at $T = 50$ MeV (dashed curves in Fig. 2). One observes clearly the competition between the increased lepton contribution due to the larger lepton=proton fractions at finite temperature, and the decrease of the nucleonic contribution due to the larger isospin symmetry. At low density the former effect is dominant, but at high density there is strong compensation between both. The overall result is a slight increase of the total thermal energy density in beta-stable matter due to the action of the weak interaction via increased lepton and proton fractions. This change is small compared to the dominant cause of temperature dependence by the strong interaction as investigated in Sec. II A.

C. Adiabatic index

An important quantity often used in NS merger simulations [26, 27, 55–57] is the adiabatic index Γ_{th} appearing in the ideal-fluid approximation

$$p_{\text{th}}(T, \rho) = (\Gamma_{\text{th}} - 1) \varepsilon_{\text{th}}(T, \rho) \quad (20)$$

with a constant Γ_{th} (originally chosen as $\Gamma_{\text{th}} \approx 1.5$ [56]). We note that due to the thermal effects analyzed before, this relation might be strongly violated in our microscopic approach, in particular for EOSs with relatively small proton fraction (UIX), where the thermal pressure might even become negative at high density. In fact, three-dimensional relativistic hydrodynamical calculations of NS mergers [27] have questioned the validity of this approximation in the postmerger phase, where thermal effects are most relevant. Strong variations were found in both the oscillation frequency of the forming hypermassive object, and the delay time between merging and black hole formation, with respect to the simulations with a fully consistent treatment of temperature.

To illustrate this issue, we show in Fig. 5 the adiabatic index $\Gamma_{\text{th}} = 1 + p_{\text{th}}/\varepsilon_{\text{th}}$ at $T = 50$ MeV derived from our results for the different EOSs. There is clearly an important density dependence (the temperature dependence turns out to be much less pronounced) and the average remains even below 1.5, in particular at high density. For comparison we also display results of some frequently used RMF models, namely the LS220 EOS [30], the Shen EOS [31], and the recent SFHo [36]. We plan to study this problem more extensively in future detailed merger simulations.

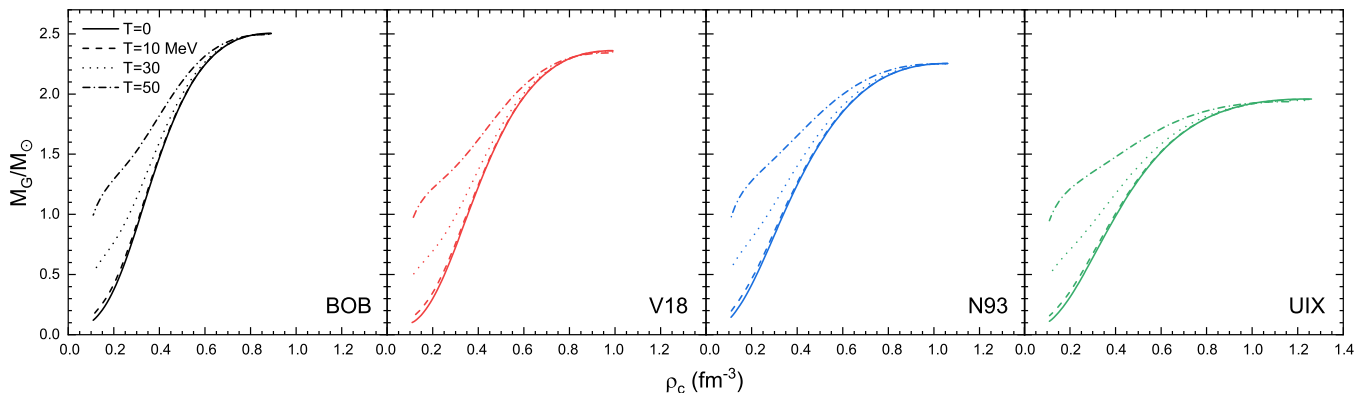


FIG. 6. Neutron star gravitational mass vs. central density relations at $T = 0, 10, 30, 50$ MeV, for the different EOSs.

D. Stellar structure

The features of the temperature-dependent EOSs are reflected in Fig. 6, where the corresponding gravitational mass vs. central density relations are plotted for isothermal stars at $T = 0, 10, 30, 50$ MeV. One notes that the theoretical predictions for the maximum masses depend most importantly on the nuclear EOS ($M_{\max}/M_{\odot} = 2.50, 2.36, 2.25, 1.96$ for BOB, V18, N93, UIX respectively), whereas the dependence on temperature is nearly negligible, and summarized in the upper panel of Fig. 7, showing the relative change of the maximum mass with temperature. There is a slight decrease, reaching about one percent at $T = 50$ MeV for the UIX EOS and less for the other, stiffer EOSs.

However, those results regard the maximum reachable gravitational mass at finite temperature, regardless of the (approximate) conservation of baryon number in the dynamical evolution. It is therefore also of interest to analyze the behavior of the maximum baryonic mass $M_B(T)$ with temperature, and this is shown in the lower panel of Fig. 7. In fact a stronger decrease (up to about 6%) is observed here, as less baryons can be bound with increasing temperature. The much weaker decrease of $M_G(T)$ relative to this behavior is due to the thermal increase of the internal energy density ϵ_{th} , which adds gravitational mass to the star.

This qualitative analysis is in agreement with the similar one performed in Ref. [38] for a number of RMF models at finite temperature, including the three models featured in Fig. 5. However, in that case and in the older potential models framework of Ref. [14] increasing maximum gravitational masses with temperature were reported. This could be caused by interactions which are mostly local with a non-local correction, as in Ref. [14], and therefore thermal effects are included only in the kinetic energy. In our calculations thermal effects are contained in the whole interaction part through the single-particle potentials; thus a completely different temperature dependence may arise. In fact the relevant adiabatic index is fairly small in our approach, see Fig. 5, while larger values in other models might be able to cause an increase of the maximum mass. This will be the subject of further study.

Finally, we remind that the effect of neutrino trapping was completely disregarded in this schematic investigation, which

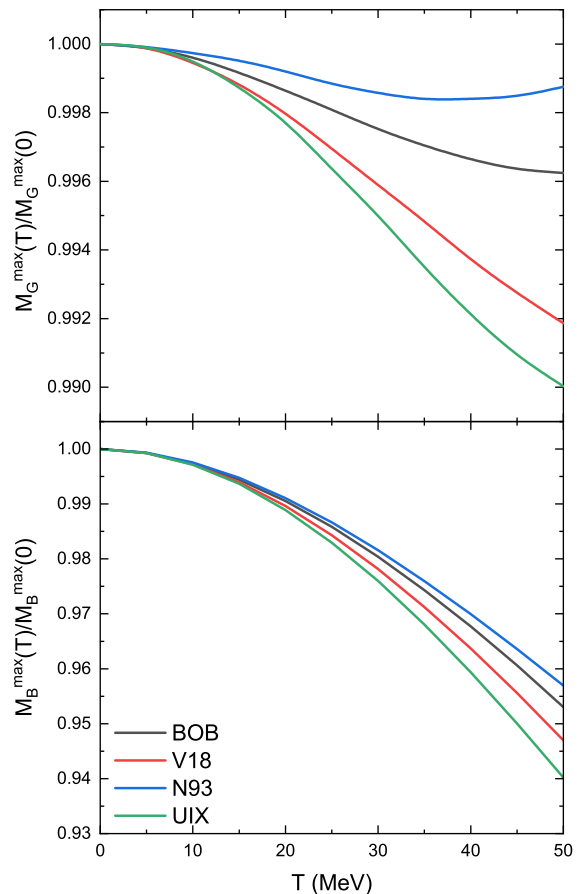


FIG. 7. Temperature dependence of the neutron star gravitational (upper panel) and baryonic (lower panel) maximum mass for the different EOSs.

focused on the temperature effects of the strong interaction. The neutrino contributions to thermal energy density and pressure might also cause a substantial increase of the maximum masses [16, 28, 29, 38]. But for a consistent analysis much more detailed simulations are required.

IV. SUMMARY

In conclusion, we presented microscopic calculations and convenient parametrizations of the equation of state of hot asymmetric nuclear matter within the framework of the Brueckner-Hartree-Fock approach at finite temperature with different potentials and compatible nuclear three-body forces. We notice that our results have been obtained in the framework of the frozen-correlations approximation scheme, but a more complete calculation is expected to give a similar behavior.

We then investigated the EOS of hot NS matter, in particular the density dependence of the adiabatic index, and determined the dependence of the maximum NS mass on temperature for beta-stable and neutrino-free configurations. At variance with other available EOSs at finite temperature, widely used in neutron star merger simulations, we found a very small maximum

mass decrease up to rather large temperatures, which can be related to the competition between increasing thermal pressures and increasing isospin symmetry of the stellar nuclear matter. This small effect would practically justify to disregard the temperature dependence of the nuclear EOS in merger simulations, as far as stellar stability is concerned. To verify this supposition, we plan to employ the various microscopic EOSs in detailed simulations to be confronted with future observations of merger events. This will allow to constrain even more the possible EOS.

ACKNOWLEDGMENTS

This work is sponsored by the National Natural Science Foundation of China under Grant Nos. 11075037, 11475045 and the China Scholarship Council, File No. 201806100066. We further acknowledge partial support from “PHAROS,” COST Action CA16214.

-
- [1] B. P. Abbott et al., Phys. Rev. Lett. **119**, 161101 (2017); **121**, 161101 (2018).
- [2] L. Baiotti and L. Rezzolla, Rep. Prog. Phys. **80**, 096901 (2017).
- [3] V. Paschalidis and N. Stergioulas, Living Reviews in Relativity **20**, 7 (2017).
- [4] K. A. Brueckner and J. L. Gammel, Phys. Rev. **109**, 1023 (1958); J. P. Jeukenne, A. Lejeune, and C. Mahaux, Phys. Rep. **25C**, 83 (1976); B. Day, Nucl. Phys. **A328**, 1 (1979).
- [5] M. Baldo, *Nuclear Methods and the Nuclear Equation of State*, International Review of Nuclear Physics, Vol. 8 (World Scientific, Singapore, 1999).
- [6] M. Baldo and G. F. Burgio, Rep. Prog. Phys. **75**, 026301 (2012).
- [7] M. Baldo, I. Bombaci, and G. F. Burgio, Astron. Astrophys. **328**, 274 (1997); X. R. Zhou, G. F. Burgio, U. Lombardo, H.-J. Schulze, and W. Zuo, Phys. Rev. **C69**, 018801 (2004).
- [8] W. Zuo, A. Lejeune, U. Lombardo, and J.-F. Mathiot, Nucl. Phys. **A706**, 418 (2002); Z. H. Li, U. Lombardo, H.-J. Schulze, and W. Zuo, Phys. Rev. **C77**, 034316 (2008).
- [9] Z. H. Li and H.-J. Schulze, Phys. Rev. **C78**, 028801 (2008).
- [10] Z.-H. Li, D.-P. Zhang, H.-J. Schulze, and W. Zuo, Chin. Phys. Lett. **29**, 012101 (2012); Q.-Y. Bu, Z.-H. Li, and H.-J. Schulze, Chin. Phys. Lett. **33**, 032101 (2016).
- [11] G. Taranto, M. Baldo, and G. F. Burgio, Phys. Rev. **C87**, 045803 (2013).
- [12] G. F. Burgio, A. Drago, G. Pagliara, H.-J. Schulze, and J.-B. Wei, Ap. J. **860**, 139 (2018); J.-B. Wei, A. Figura, G. F. Burgio, H. Chen, and H.-J. Schulze, J. Phys. **G46**, 034001 (2019).
- [13] A. Burrows and J. M. Lattimer, Astrophys. J. **307**, 178 (1986).
- [14] M. Prakash, I. Bombaci, M. Prakash, P. J. Ellis, J. M. Lattimer, and R. Knorren, Phys. Rep. **280**, 1 (1997).
- [15] J. A. Pons, S. Reddy, M. Prakash, J. M. Lattimer, and J. A. Miralles, Astrophys. J. **513**, 780 (1999); L. Villain, J. A. Pons, P. Cerdá-Durán, and E. Gourgoulhon, Astron. Astrophys. **418**, 283 (2004).
- [16] O. E. Nicotra, M. Baldo, G. F. Burgio, and H.-J. Schulze, Astron. Astrophys. **451**, 213 (2006); Phys. Rev. **D74**, 123001 (2006); A. Li, X. R. Zhou, G. F. Burgio, and H.-J. Schulze, Phys. Rev. **C81**, 025806 (2010); G. F. Burgio, H.-J. Schulze, and A. Li, Phys. Rev. **C83**, 025804 (2011).
- [17] G. F. Burgio and H.-J. Schulze, Astron. Astrophys. **518**, A17 (2010).
- [18] H. A. Bethe, Rev. Mod. Phys. **62**, 801 (1990).
- [19] P. B. Demorest, T. Pennucci, S. M. Ransom, M. S. E. Roberts, and J. W. T. Hessels, Nature **467**, 1081 (2010); J. A. Antoniadis et al., Science **340**, 6131 (2013); E. Fonseca et al., Astrophys. J. **832**, 167 (2016).
- [20] H. T. Cromartie et al., arXiv:1904.06759.
- [21] M. Shibata et al., Phys. Rev. **D96**, 123012 (2017); B. Margalit and B. D. Metzger, Astrophys. J. **850** L19 (2017); L. Rezzolla, E. R. Most, and L. R. Weih, Astrophys. J. **852** L25 (2018); M. Ruiz, S. L. Shapiro, and A. Tsokaros, Phys. Rev. **D97**, 021501(R) (2018).
- [22] M. Hashimoto, K. Oyamatsu, and Y. Eriguchi, Astrophys. J. **436**, 257 (1994).
- [23] J. O. Goussard, P. Haensel, and J. L. Zdunik, Astron. Astrophys. **321**, 822 (1997).
- [24] K. Strobel, C. Schaab, and M. K. Weigel, Astron. Astrophys., **350**, 497 (1999); K. Strobel, M. K. Weigel, Astron. Astrophys., **367**, 582 (2001).
- [25] G. F. Burgio, H.-J. Schulze, and F. Weber, Astron. Astrophys. **408**, 675 (2003).
- [26] L. Baiotti, B. Giacomazzo, and L. Rezzolla, Phys. Rev. **D78**, 084033 (2008); K. Hotokezaka, K. Kyutoku, H. Okawa, M. Shibata, and K. Kiuchi, Phys. Rev. **D83**, 124008 (2011); A. Endrizzi, R. Ciolfi, B. Giacomazzo, W. Kastaun, and T. Kawamura, Class. Quantum Grav. **33**, 164001 (2016); M. Hanauske, K. Takami, L. Bovard, L. Rezzolla, J. A. Font, F. Galeazzi, and H. Stöcker Phys. Rev. **D96**, 043004 (2017); D. Radice, A. Perego, S. Bernuzzi, and B. Zhang, MNRAS **481**, 3670 (2018); D. Radice, A. Perego, K. Hotokezaka, S. A. Fromm, S. Bernuzzi, and L. F. Roberts, Astrophys. J. **869**, 130 (2018); M. G. Alford, L. Bovard, M. Hanauske, L. Rezzolla, and K. Schwenzer, Phys. Rev. Lett. **120**, 041101 (2018).
- [27] A. Bauswein, H.-T. Janka, and R. Oechslin, Phys. Rev. **D82**, 084043 (2010).

- [28] V. Paschalidis, Z. B. Etienne, and S. L. Shapiro, Phys. Rev. **D86**, 064032 (2012).
- [29] S. Lalit, M. A. A. Mamun, C. Constantinou, and M. Prakash, Eur. Phys. J. **A55**, 10 (2019).
- [30] J. M. Lattimer and F. D. Swesty, Nucl. Phys. **A535**, 331 (1997); <http://www.astro.sunysb.edu/lattimer/EOS/main.html>
- [31] H. Shen, H. Toki, K. Oyamatsu, and K. Sumiyoshi, Nucl. Phys. **A637**, 435 (1998); Prog. Theor. Phys. **100**, 1013 (1998).
- [32] M. Hempel and J. Schaffner-Bielich, Nucl. Phys. **A837**, 210 (2010).
- [33] S. Typel, G. Röpke, T. Klähn, D. Blaschke, and H. H. Wolter, Phys. Rev. **C81**, 015803 (2010).
- [34] G. Shen, C. J. Horowitz, and S. Teige, Phys. Rev. **C83**, 035802 (2011).
- [35] G. Shen, C. J. Horowitz, and E. O'Connor, Phys. Rev. **C83**, 065808 (2011).
- [36] A. W. Steiner, M. Hempel, and T. Fischer, Ap. J. **774**, 17 (2013).
- [37] T. W. Baumgarte, S. L. Shapiro, and S. A. Teukolsky, Ap. J. **458**, 680 (1996).
- [38] J. D. Kaplan, C. D. Ott, E. P. O'Connor, K. Kiuchi, L. Roberts, and M. Duez, Ap. J. **790**, 19 (2014).
- [39] C. Bloch and C. De Dominicis, Nucl. Phys. **7**, 459 (1958); **10**, 181,509 (1959).
- [40] A. Lejeune, P. Grangé, M. Martzloff, and J. Cugnon, Nucl. Phys. **A453**, 189 (1986).
- [41] M. Baldo and L. S. Ferreira, Phys. Rev. **C59**, 682 (1999).
- [42] R. B. Wiringa, V. G. J. Stoks, and R. Schiavilla, Phys. Rev. **C51**, 38 (1995).
- [43] R. Machleidt, K. Holinde, and Ch. Elster, Phys. Rep. **149**, 1 (1987); R. Machleidt, Adv. Nucl. Phys. **19**, 189 (1989).
- [44] M. M. Nagels, T. A. Rijken, and J. J. de Swart, Phys. Rev. **D17**, 768 (1978); V. G. J. Stoks, R. A. M. Klomp, C. P. F. Terheggen, and J. J. de Swart, Phys. Rev. **C49**, 2950 (1994).
- [45] P. Grangé, A. Lejeune, M. Martzloff, and J.-F. Mathiot, Phys. Rev. **C40**, 1040 (1989).
- [46] J. Carlson, V. R. Pandharipande, and R. B. Wiringa, Nucl. Phys. **A401**, 59 (1983); R. Schiavilla, V. R. Pandharipande, and R. B. Wiringa, Nucl. Phys. **A449**, 219 (1986).
- [47] I. Bombaci and U. Lombardo, Phys. Rev. **C44**, 1892 (1991); W. Zuo, I. Bombaci, and U. Lombardo, Phys. Rev. **C60**, 024605 (1999).
- [48] See Supplemental Material at [URL will be inserted by publisher].
- [49] M. G. Alford and S. P. Harris, Phys. Rev. **C98**, 065806 (2018).
- [50] S. L. Shapiro and S. A. Teukolsky, *Black Holes, White Dwarfs, and Neutron Stars* (John Wiley and Sons, New York, 1983).
- [51] J. W. Negele and D. Vautherin, Nucl. Phys. **A207**, 298 (1973).
- [52] G. Baym, C. Pethick, and D. Sutherland, Astrophys. J. **170**, 299 (1971).
- [53] R. Feynman, F. Metropolis, and E. Teller, Phys. Rev. **C75**, 1561 (1949).
- [54] M. Fortin, G. Taranto, G. F. Burgio, P. Haensel, H.-J. Schulze, and J. L. Zdunik, MNRAS **475**, 5010 (2018); J.-B. Wei, G. F. Burgio, and H.-J. Schulze, MNRAS **484**, 5162 (2019).
- [55] A. Endrizzi, D. Logoteta, B. Giacomazzo, I. Bombaci, W. Kastaun, and R. Ciolfi, Phys. Rev. **D98**, 043015 (2018).
- [56] H.-T. Janka, T. Zwerger, and R. Moenchmeyer, Astron. Astrophys. **268**, 360 (1993).
- [57] C. A. Raithel, F. Özel, and D. Psaltis, Ap. J. **875**, 12 (2019).